



## Maximize CdTe solar cell performance through copper activation engineering

Deng-Bing Li, Sandip S. Bista, Zhaoning Song, Rasha A. Awni, Kamala K. Subedi, Niraj Shrestha, Puja Pradhan, Lei Chen, Ebin Bastola, Corey R. Grice, Adam B. Phillips, Michael J. Heben, Randy J. Ellingson, Yanfa Yan<sup>\*\*</sup>

Department of Physics and Astronomy, and Wright Center for Photovoltaics Innovation and Commercialization (PVIC), University of Toledo, Toledo, OH, 43606, USA

### ABSTRACT

The incorporation of copper (Cu) is one of the critical processes for fabricating high-efficiency CdTe thin-film solar cells. However, due to its high mobility in CdTe, the distribution and concentration of Cu must be carefully engineered to reduce the compensative donor-like interstitial defects in CdTe bulk and the recombination centers at the buffer layer/CdTe interface to maximize device performances. Here, a cuprous chloride (CuCl) solution treatment and a rapid thermal annealing (RTA) process are used to control the concentration and distribution of Cu in CdTe absorbers, enabling a champion CdTe thin-film solar cell with a power conversion efficiency of 17.5% without selenium incorporation. The results demonstrate that the use of a CuCl solution can substantially reduce the amount of Cu needed in CdTe and the RTA process is a viable approach to engineer the Cu distribution in CdTe solar cells.

### 1. Introduction

In the past decade, cadmium telluride (CdTe) solar cell technology has attracted great attention in the photovoltaic market due to its low cost and high efficiency [1,2]. The First Solar Inc. has delivered the world-record power conversion efficiencies (PCEs) of 22.1% and over 19% for CdTe cells and modules, respectively [3]. However, due to the high electron affinity of CdTe, forming a good ohmic contact between CdTe and the metal electrode remains a crucial challenge for most researchers. One of the common procedures to improve the ohmic contact is to improve the carrier concentration at the CdTe back surface through copper (Cu) doping.

Over the years, significant efforts have been devoted to the Cu doping on CdS/CdTe solar cells [4–6]. Cu has been involved in CdTe solar cells since the pioneering work by Adirovich and co-workers in 1969 [7]. It is well known that Cu can increase the p-type conductivity of CdTe by occupying the Cd site ( $\text{Cu}_{\text{Cd}}$ ) and thereby reduce the Shottky barrier between CdTe and Au [8,9]. However, there are still two major concerns about the dynamic behavior of Cu in CdTe. The first is that the solubility of Cu atoms in CdTe grain interiors is below  $3 \times 10^{14}$  atoms  $\text{cm}^{-3}$ , which is comparable with the highest carrier concentration that can be achieved through Cu doping, but far below the desired carrier concentration value of  $10^{16} \sim 10^{17}$   $\text{cm}^{-3}$  [10,11]. Nonetheless, the actual Cu concentration researchers applied to the CdTe films is at least five

orders of magnitude higher than the final carrier concentration, indicating a low utility ratio of Cu [9]. For example, a 3–4 nm thick Cu layer deposited on 3–4  $\mu\text{m}$  CdTe films provides an average Cu concentration of  $\sim 8.5 \times 10^{19}$  atoms  $\text{cm}^{-3}$  [12]. This results in not only the segregation of excess Cu atoms to grain boundaries, but also the formation of interstitial defects ( $\text{Cu}_i$ ) which has been known to act as donors with a high diffusivity [13,14]. The higher dose of Cu could introduce several hundred thousand times more compensative donor-like defects at grain boundaries than the  $\text{Cu}_{\text{Cd}}$  acceptors in the bulk, which has been observed by transmission electron microscopy (TEM) measurements [13]. When Cu dopants are introduced into CdTe, they first diffuse into the Cd vacancies ( $\text{V}_{\text{Cd}}$ ), forming the substitutional  $\text{Cu}_{\text{Cd}}$  acceptors due to its low formation energy [8,15]. However, as a significantly larger number of Cu atoms are introduced into a CdTe film, the Fermi level of CdTe moves towards the valence band maximum. In such a case, the formation energy of the charged donor defect  $\text{Cu}_i^+$  decreases linearly as a function of the Fermi energy, and a high concentration of  $\text{Cu}_i^+$  donors generated with the increasing Cu dosage, reducing the net hole concentration [15]. Thus, the p-type conductivity is limited due to these compensative effects [9]. To maximize the hole density in CdTe, the Cu concentration in CdTe should be carefully controlled to the level of the solubility of Cu in CdTe ( $3 \times 10^{13} \sim 3 \times 10^{14}$  atoms  $\text{cm}^{-3}$ ).

The second concern is the high mobility of Cu in CdTe films. Cu does not always localize at the rear of CdTe but diffuses at a relatively fast

\* Corresponding author.

E-mail address: [yanfa.yan@utoledo.edu](mailto:yanfa.yan@utoledo.edu) (Y. Yan).

<https://doi.org/10.1016/j.nanoen.2020.104835>

Received 3 March 2020; Received in revised form 2 April 2020; Accepted 8 April 2020

Available online 17 April 2020

2211-2855/© 2020 Elsevier Ltd. All rights reserved.

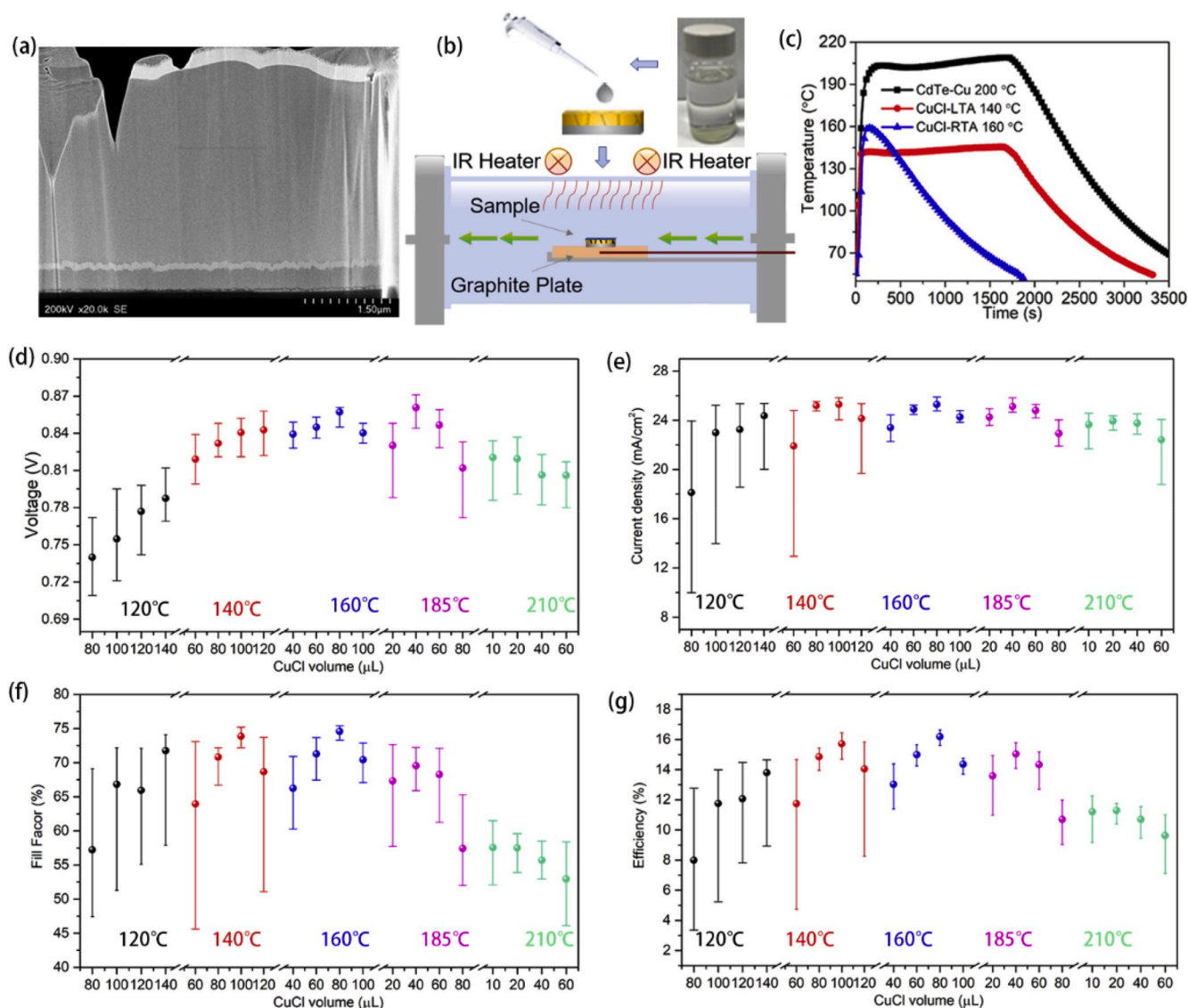


**Fig. 1.** (a) Cross-sectional TEM image of a complete ZMO/CdTe device. (b) Solution-processed CuCl treatment procedure. (c) Annealing temperature profiles for ZMO/CdTe solar cells with metallic Cu and CuCl with LTA and RTA treatment. (d)–(g) Statistical results for MZO/CdTe solar cell performances with different CuCl annealing temperatures and CuCl solution volumes in RTA treatment.

speed to the buffer layer/CdTe interface and even into the buffer layer [16,17]. The secondary ion mass spectroscopy (SIMS) depth profile of our CdTe device with 3 nm thermal evaporated Cu annealed at 200 °C for 20 min shows a clear aggregation of Cu at the buffer layer/CdTe interface (Figure S1). Both simulation and experiment results have shown that the diffusion constant of Cu in CdTe is about  $1 \times 10^{-2} \mu\text{m}^2 \text{s}^{-1}$  at 200 °C, corresponding to a more than 2  $\mu\text{m}$  diffusion distance in 2 min [9]. Even at room temperature, the same diffusion distance needs only  $\sim 1$  day [9]. The fast diffusion of Cu and its accumulation at the front junction have been observed by many researchers [18–20]. The aggregation of Cu at the CdS/CdTe interface introduces recombination centers and shunt pathways, causing the degradation of device performance [20]. Therefore, a well-controlled Cu distribution in CdTe is necessary to maximize device efficiency as well as long-time stability.

To control the concentration and distribution of Cu, many approaches have been investigated, such as using Cu compounds,  $\text{Cu}_x\text{Te}$  [21–23] or Cu doped ZnTe [24,25]. However, many devices showed relatively low performances due to the difficulty of the  $\text{Cu}_x\text{Te}$  phase control and the low ZnTe conductivity. Recently, copper chloride ( $\text{CuCl}_2$ ) was investigated as the Cu source in CdTe solar cells to avoid the

diffusion of Cu into the front junction. However, moderate PCEs of  $\sim 16\%$  were obtained [12,26]. Sites, Sampath, and coworkers have demonstrated a PCE of 18.7% using sublimated cuprous chloride ( $\text{CuCl}$ ) to facilitate the Cu diffusion [1,27–29]. However, the requirements for accurate control of CuCl amount and an oxygen-free atmosphere limit the flexibility for wide application due to the low Cu dosage needed in CdTe and the high sensitivity of CuCl powders to oxygen during deposition. In this work, we develop a wet chemical method to introduce CuCl into zinc magnesium oxide (ZMO)/CdTe devices. This method can be processed in ambient conditions and provides a way to substantially reduce the amount of Cu needed in CdTe. Benefiting from these advantages, a PCE of 17.5% is achieved for ZMO/CdTe devices without selenium incorporation, which is close to the reported record efficiency of 18.7% for ZMO/CdTe devices [27].

## 2. Experimental

### 2.1. Device fabrication

The devices are fabricated in the schematic as shown in Fig. 1b.

Fluorine doped tin oxide (FTO) coated glass (TEC 12; Pilkington NA) is used as the substrate for fabricating CdTe solar cells. The substrates are first cleaned with Micro-90 detergent in hot water ( $\sim 70^\circ\text{C}$ ) in an ultrasonic bath for an hour, followed with 4 times ultrasonic bath in deionized water for 30 min. After that, the substrates are rinsed with deionized water and dried with nitrogen. An 80 nm ZMO buffer layer is then deposited on FTO substrates at room temperature by radio-frequency sputtering under a mixed flow gas of 3% oxygen and 97% argon using a commercial ZMO target with 8 wt% magnesium oxide. ZMO films are cleaned by UV-ozone treatment for 10 min. Then, a  $\sim 3.5\ \mu\text{m}$  CdTe is deposited by close space sublimation (CSS) with a source temperature of  $560^\circ\text{C}$  and a substrate temperature of  $495^\circ\text{C}$  at 1 Torr. A saturated  $\text{CdCl}_2$  in methanol solution is dropped and spread on CdTe films, and then activated at  $420^\circ\text{C}$  for 20 min with a 500 sccm helium flow. After cooling to room temperature, excess  $\text{CdCl}_2$  is removed by rinsing with methanol.

CuCl solution is prepared by dissolving CuCl powders in 20 ml of ethanol followed by an ultrasonic treatment for 2 min. Note that CuCl should be oversaturated, as evidenced by the undissolved CuCl particles at the bottom of the solution (Fig. 1b). The transparent supernatant fluid with light yellow color should be used for the CuCl treatment within 1 day or otherwise should be stored in inert atmosphere to avoid degradation. For the devices with the CuCl treatment, different volumes of saturated CuCl solution are dropped onto the CdTe surface. The films are then annealed following two different methods as shown in Fig. 1c: a long time (20 min) thermal annealing (LTA) and short-time thermal annealing (RTA) at different temperatures. Then, 40 nm Au is deposited by thermal evaporation via a shadow mask with an individual cell area of  $0.08\ \text{cm}^2$ . For the devices treated by metallic Cu, after  $\text{CdCl}_2$  treatment, a bilayer of Cu ( $\sim 3\ \text{nm}$ ) and Au (40 nm) are deposited by thermal evaporation via a shadow mask with an individual cell area of  $0.08\ \text{cm}^2$ . Then, the devices are annealed in nitrogen at  $200^\circ\text{C}$  for 20 min to promote Cu doping in CdTe. 120 nm magnesium fluoride anti-reflective layer is deposited in an e-beam system.

## 2.2. Measurement and characterization

The cross-sectional microstructures of the CdTe films are characterized by a Hitachi 2300A scanning transmission electron microscope (STEM, Hitachi Inc., Japan). The TEM sample is prepared via a focused ion beam (FIB) technique using a Quanta dual-beam electron microscope (FEI Inc., USA); Pt is employed as the protective covering on the film during this process. Solar cell performance is characterized by measuring current density-voltage (J-V) curves under AM1.5G illumination using a solar simulator (PV Measurements Inc.) and a source meter (Keithley 2400). TOF-SIMS is performed using TOF-SIMS5 from ION-TOF GmbH. (Munster, Germany). Samples are analyzed in a dual beam profiling mode. The primary ion for analysis is 30 KeV  $\text{Bi}^{3+}$  (Bi liquid metal ion source). This ion beam is applied over a  $100\ \mu\text{m} \times 100\ \mu\text{m}$  area at the center of the sputter crater. Spectral data are acquired in a high mass-resolution mode. The sputter ion is 1 keV  $\text{Ar}^+$  (Ar, electron impact ion source). A  $400\ \mu\text{m} \times 400\ \mu\text{m}$  sputter crater is used. Temperature-dependent current-voltage (J-V-T) and thermal admittance spectroscopy (TAS) measurements are performed using a Solartron Modulab potentiostat equipped with a frequency response analyzer (Ametek Inc.). The capacitance voltage (C-V) and TAS measurements are performed under a constant AC modulation voltage of 45 mV. The J-V-T measurements are performed in dark with voltage sweeping from -0.4 to 1.2 V. The C-V measurements are performed in dark with a constant AC frequency of 20 kHz and a DC bias voltage varying from -2.0 to 0.75 V. The TAS measurements are done with frequency sweeping from 1.0 MHz to 0.1 Hz and DC bias varying from -0.3 to 0.2 V at a step size of 0.1 V. A liquid nitrogen cooling cryo-system (Janis VPF-100 system) is used to carry out all the temperature-dependent (150 to 300 K with a step size of 10 K) measurements. The temperature is controlled by a temperature controller (Lakeshore 330). A sensor is

mounted on the top of the device directly, to ensure that the recorded temperature is the device temperature. Photoluminescence (PL) characteristics of the devices with LTA and RTA treatment are investigated utilizing steady-state and time-resolved PL. Steady-state PL measurement is performed utilizing a 532 nm continuous wave laser at  $\sim 5\ \text{W cm}^{-2}$  excited through the FTO side. The PL signal is detected by a liquid nitrogen cooled symphony-II Si (CCD) detector after a Horiba iHR320 monochromator. Inductively coupled plasma mass spectrometry (ICP-MS) is performed for the saturated Cu(I)Cl solution using X Series 2 ICP-MS instrument (Thermo Fisher Scientific, Waltham, MA, USA). Standards and internal standards are prepared in the lab by using the certified ICP-MS standards from Inorganic Ventures (Christiansburg, VA, USA). The sample is analyzed for multiple times (at least 5 times for each sample). A thorough rinsing is carried out between sample and standards to limit cross contamination. Internal standards (added to the sample and standard solutions) are used to correct any variability in sample introduction caused by the auto sampler, plasma uptake, the cones, and ablation rate by the laser. To accurately measure quantification limits in the samples, a laboratory blank is added and processed the exactly the same way as the samples, so that possible contamination from the solvents or containers can be quantified by applying blank corrections to the sample. A pair of standards is periodically analyzed as unknown throughout an analytical session to monitor the instrumental drift.

## 3. Results and discussions

ZMO films with a band gap of 3.67 eV (Fig. S2) is used as the emitter to replace the traditional CdS. [29,30]. In the TEM image (Fig. 1a), the CdTe film shows large columnar grains with a size of  $\sim 5\ \mu\text{m}$  throughout the 3.5  $\mu\text{m}$  thickness, indicating a high-quality CdTe absorber layer. This can be attributed to the high temperature  $\text{CdCl}_2$  treatment at  $420^\circ\text{C}$ . The use of ZMO allows the  $\text{CdCl}_2$  treatments at temperatures higher than  $390^\circ\text{C}$ , which helps to improve the crystallinity of CdTe films. Furthermore, the TEM image shows a clear ZMO/CdTe interface without observable voids and pinholes, indicating high heterojunction quality without obvious inter-diffusion. In contrast, there are observable voids at CdS/CdTe interface when the  $\text{CdCl}_2$  treatment temperature is higher than  $400^\circ\text{C}$  due to the inter-diffusion, as shown in Fig. S3. After  $\text{CdCl}_2$  treatment, different Cu activation procedures are applied to ZMO/CdTe stacks following the procedures as shown in Fig. 1b and c. Two kinds of temperature profiles (LTA and RTA) are used for CuCl treatment. For the reference cell, a thin (3 nm) Cu metal layer is evaporated on CdTe films after the  $\text{CdCl}_2$  treatment, and an activation annealing process is carried out at  $200^\circ\text{C}$  for 20 min to enhance the back-contact following a temperature profile shown in Fig. 1c. This annealing treatment is used to process CdS/CdTe solar cells with an average efficiency of over 15% [31]. However, our ZMO/CdTe devices with Cu metal treatment (referred to as CdTe-Cu) show a low efficiency of 12.9%, with a  $V_{\text{OC}}$  of 0.837 V, a  $J_{\text{SC}}$  of  $24.9\ \text{mA cm}^{-2}$ , and a fill factor (FF) of 61.8% (Fig. S4), which is inferior to the performance of CdTe-CuCl devices.

For devices with CuCl treatment, both LTA and RTA annealing procedures are applied on ZMO/CdTe devices (named CuCl-LTA and CuCl-RTA, respectively, hereafter) to control the distribution of Cu in CdTe films. According to our optimization for the RTA treatment (Fig. 1d-g and Fig. S5), the  $V_{\text{OC}}$  increases gradually from around 0.750 to 0.870 V when the annealing temperature increases from 120 to  $160^\circ\text{C}$  due to the facilitated Cu diffusion at higher temperatures. However, when the annealing temperature is further increased to  $210^\circ\text{C}$ ,  $V_{\text{OC}}$  value decreases significantly to an average value of 0.825 V due to the over diffusion of Cu. The highest FF of over 75% is observed in CuCl-RTA devices when the annealing temperatures are 140 and  $160^\circ\text{C}$ , indicating that the performance of  $V_{\text{OC}}$  is dominated by the Cu concentration in CdTe bulk while the FF is dominated by the Cu concentration at CdTe back surface. Comparing with the pronounced variation in  $V_{\text{OC}}$  and FF, the maximum  $J_{\text{SC}}$  at different annealing temperatures varies slightly,

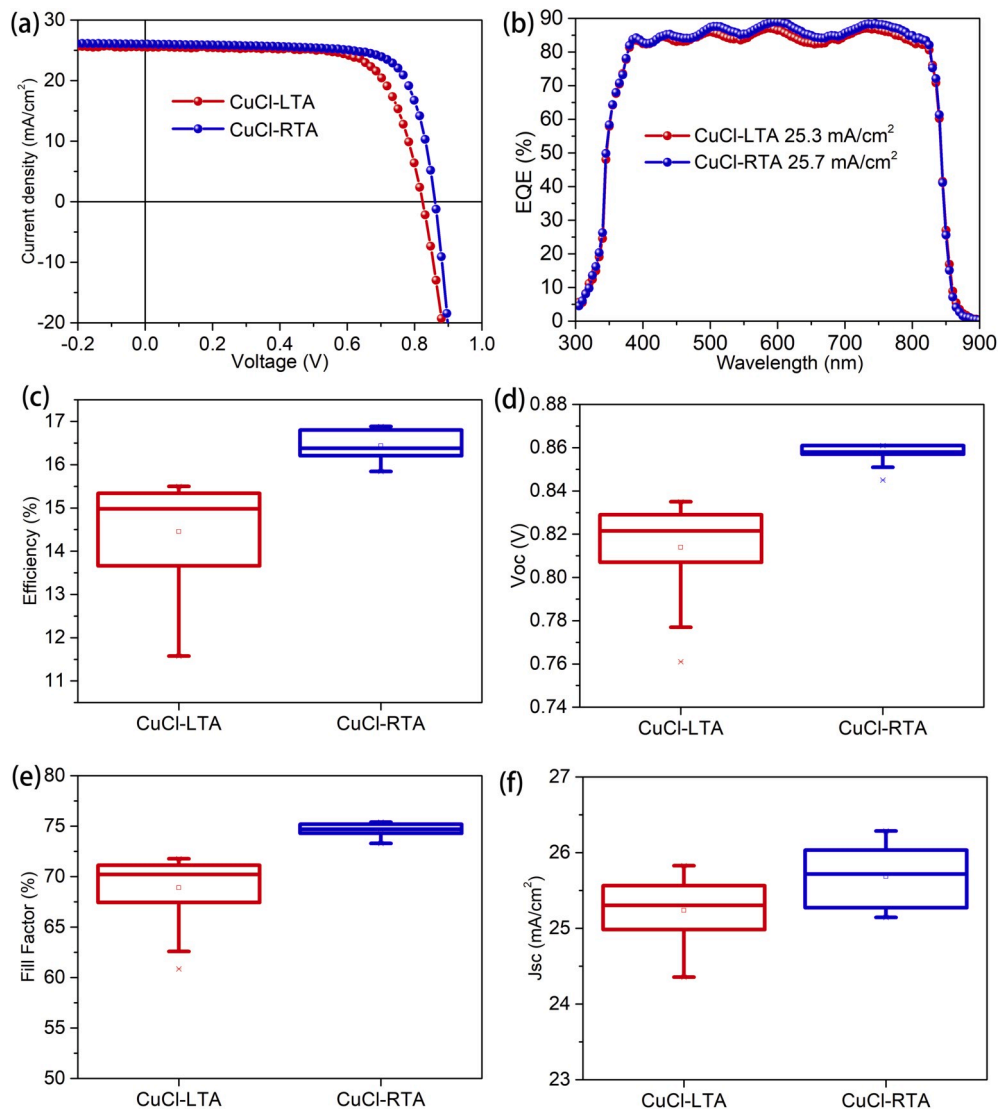


**Fig. 2.** (a) J-V and (b) EQE curves of the champion devices with the LTA and RTA CuCl treatments. Statistical comparison of (c) efficiency, (d)  $V_{OC}$ , (e) fill factor and (f)  $J_{SC}$  of MZO/CdTe devices with the LTA and RTA CuCl treatments.

with the peak  $J_{SC}$  value of 25.9 mA cm<sup>-2</sup> achieving at 160 °C. In addition, when the devices are treated at 160 °C, the device performances show a much tighter distribution, indicating higher reproducibility. The effect of CuCl solution volume on device performances varies on the RTA temperature: at low RTA temperatures (120 °C, 140 °C, e.g.), more CuCl solution produces higher device performance, especially higher  $V_{OC}$ ; at high RTA temperatures, less CuCl solution produces better device performances due to the high mobility of Cu at higher temperatures. Our capacitance-voltage (C-V) measurements track the carrier density changes in CdTe film while different CuCl solution volumes are applied (Fig. S6). Following the variations in  $V_{OC}$ , FF and  $J_{SC}$ , the highest overall efficiency for the CuCl-RTA devices is 16.8%, with a  $V_{OC}$  of 0.860 V, a  $J_{SC}$  of 25.9 mA cm<sup>-2</sup>, and a FF of 75.4%, achieved at the conditions of 160 °C annealing temperature and 80  $\mu$ L CuCl solution. For the CuCl-LTA samples, the optimized activation treatment is 140 °C for 20 min with an 80  $\mu$ L CuCl solution. As the annealing treatment temperature increases,  $V_{OC}$  increases and series resistance ( $R_S$ ) decreases gradually (Fig. S7) due to the improvement of Cu doping concentration at higher temperatures. However, the FF shows the highest value when the devices are annealed at 140 °C, indicating a proper Cu concentration that enables the highest carrier extraction and collection efficiencies. The increase of the CuCl solution volume produces higher  $V_{OC}$  until the

volume reaches 100  $\mu$ L (Fig. S8). FF and  $J_{SC}$  show the highest values accompanied with the lowest  $R_S$  and highest  $R_{SH}$  when an 80  $\mu$ L CuCl solution is applied.

The champion devices with LTA and RTA treatments are compared in Fig. 2. The best CuCl-RTA device shows clearly improved  $V_{OC}$  and FF values compared to our best CuCl-LTA device. The best CuCl-LTA device delivers an efficiency of 15.0%, with a  $V_{OC}$  of 0.829 V, a  $J_{SC}$  of 25.5 mA cm<sup>-2</sup>, and a FF of 71.1%, while the CuCl-RTA device delivers an efficiency of 16.8% with a  $V_{OC}$  of 0.860 V, a  $J_{SC}$  of 25.9 mA cm<sup>-2</sup>, and a FF of 75.4%. Both devices show similar EQE profiles with high photon responses at wavelengths between 375 and 825 nm as shown in Fig. 2b. The CuCl-RTA device shows clearly higher quantum efficiencies in both short and long wavelength ranges. This suggests the improved ZMO/CdTe junction quality and reduced back-barrier in the CuCl-RTA device compared to the CuCl-LTA device, and thus, higher carrier transport and extract efficiencies. The statistical performances of the CuCl-LTA and CuCl-RTA devices (20 cells in each group) are compared in Fig. 2c-f. Besides higher performance, it is noted that the CuCl-RTA devices show a tighter performance distribution than CuCl-LTA devices, especially the  $V_{OC}$  and efficiencies, indicating better reproducibility. For the champion devices with the LTA and RTA treatment,  $R_S$ ,  $R_{SH}$ , ideality diode factor (A), and saturation current density ( $J_0$ ) are extracted from the J-V curves

**Table 1**

Device performance parameters of the champion devices with the metallic Cu and CuCl with the LTA and RTA treatments.

Devices	$V_{OC}$ (V)	$J_{SC}$ (mA $cm^{-2}$ )	FF (%)	PCE (%)	$R_S$ ( $\Omega$ $cm^2$ )	$R_{SH}$ ( $\Omega$ $cm^2$ )	A	$J_0$ ( $\times$ $10^{-6}$ mA $cm^{-2}$ )
CuCl- LTA	0.829	25.5	71.1	15.0	2.41	1280	1.47	5.00
CuCl- RTA	0.860	25.9	75.2	16.8	1.81	1790	1.38	1.20

according to Sites' method (Table 1) [32]. The CuCl-RTA device shows a  $R_S$  of  $1.81 \Omega cm^2$ , which is much lower than the  $R_S$  of  $2.41 \Omega cm^2$  for the CuCl-LTA device. Compared with the CuCl-LTA device, the CuCl-RTA device shows a shunt resistance improvement from  $1270 \Omega cm^2$  to  $1790 \Omega cm^2$ , contributing to the improvement of FF from 71.1 to 75.2%. Besides, the CuCl-LTA device shows a higher A value of 1.47 than that of 1.38 for the CuCl-RTA device.  $J_0$  is reduced from  $5.0 \times 10^{-6} mA cm^{-2}$  for the CuCl-LTA device to  $1.2 \times 10^{-6} mA cm^{-2}$  for the CuCl-RTA device. The reductions of A and  $J_0$  values represent the reduction of the heterojunction nonradiative recombination. In addition, lower  $J_0$  can help to improve device  $V_{OC}$  according to the equation:

$$V_{OC} = \frac{AK_B T}{q} \ln \left( \frac{J_{SC}}{J_0} + 1 \right) \quad (1)$$

where  $k_B$  is the Boltzmann constant,  $q$  the unit charge, and  $T$  the Kelvin temperature.

Secondary ion mass spectroscopy (SIMS) depth profiles are introduced to probe the distribution of Cu in the CuCl-LTA and CuCl-RTA devices. SIMS has been widely used in solar cell characterization for mapping the atomic distribution due to its low detection limit. For facile comparison, the distribution profiles of Cu in the CuCl-LTA and CuCl-RTA devices are plotted together in Fig. 3a. At the back surface of

CdTe absorbers, the CuCl-LTA device shows lower Cu intensities as compared to the CuCl-RTA device, indicating a lower Cu concentration at the back surface. This mainly affects the back-barrier height, which will be confirmed later. Since the same amount of CuCl is used in these two devices, a lower Cu concentration at the back of the CuCl-LTA device suggests more Cu diffused into the CdTe bulk, and even the front interface. This is confirmed by the spike of the Cu profile at the ZMO/CdTe interface of the CuCl-LTA device. In contrast, the CuCl-RTA device shows an almost flat Cu profile at the ZMO/CdTe interface. The reduced copper concentration at the front interface of the CuCl-RTA device is mainly attributed to the short annealing duration, as shown in Fig. 1c. The diffusion of Cu into the front interface has been widely reported in CdS/CdTe devices [18,20,33,34]. A. Balcioğlu found that the density of Cu related deep donor defect complexes near or at the front interface increases sharply with the concentration of Cu, which significantly limits the carrier lifetime [33]. In addition, the aggregated Cu at the ZMO/CdTe interface can diffuse into ZMO and form acceptor-like defects, which would significantly decrease the conductivity in ZMO films as reported in the literature [35–37]. Lower ZMO conductivity results in a higher barrier for electron transport through the ZMO layer to the FTO electrode, thus, resulting in lower FF and device performances [38]. This can be further confirmed in the devices with a 3 nm evaporated metallic Cu layer, in which a higher Cu concentration at the ZMO/CdTe interface is observed (Fig. S1) after annealing at  $200^\circ C$  for 20 min. As shown in the J-V curve in Fig. S4, a clear S-kink can be observed under forward bias near  $V_{OC}$ , which is caused by the low conductivity of ZMO film and a large front barrier at the ZMO/CdTe interface [38].

PL measurements are carried out for CuCl-LTA and CuCl-RTA devices using a 532 nm laser excitation illuminated from both the glass and CdTe sides to monitor the effect of Cu on carrier lifetime at the ZMO/CdTe interface and the back surface. As shown in Fig. 3b, both samples show PL spectra with main emission peaks centered at  $1.506 \pm 0.005 eV$  but different emission intensities. Stronger PL intensities from the glass side than the CdTe side indicates the effect of passivation on the CdTe films

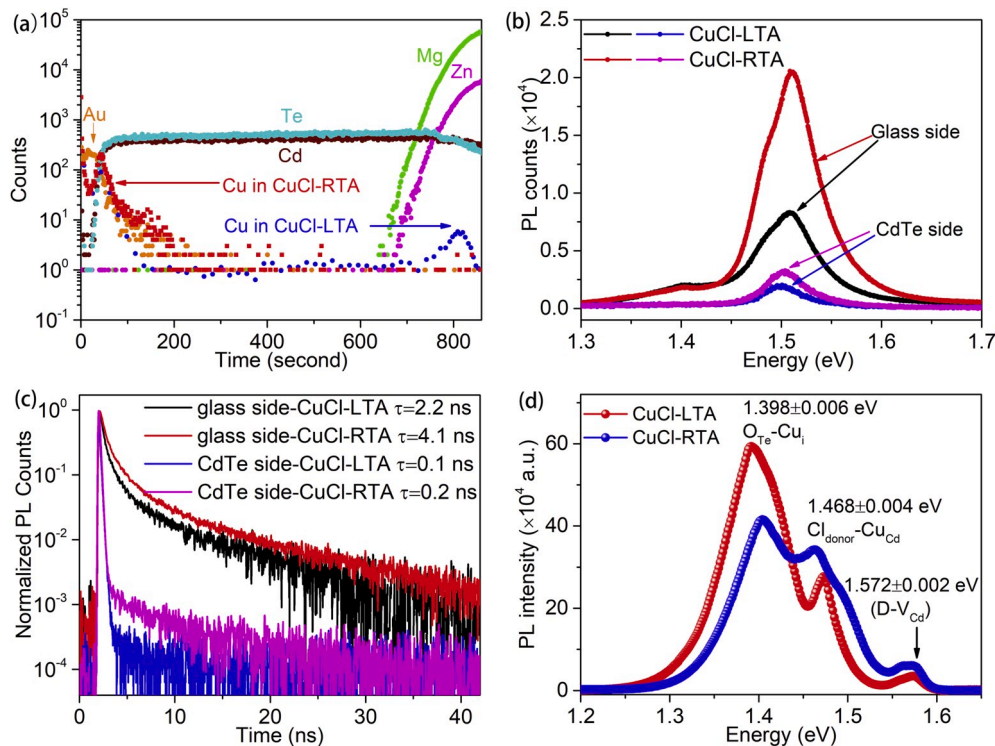


**Fig. 3.** (a) Secondary ion mass spectroscopy (SIMS) depth profiles of the CuCl-LTA and CuCl-RTA devices. (b) Steady-state PL and (c) TRPL spectra of FTO/MZO/CdTe samples with the LTA and RTA treatments. (d) PL spectra of CuCl-LTA and CuCl-RTA devices at 9 K. For each sample, PL spectra are excited through the FTO/MZO side with a 532 nm laser excitation.

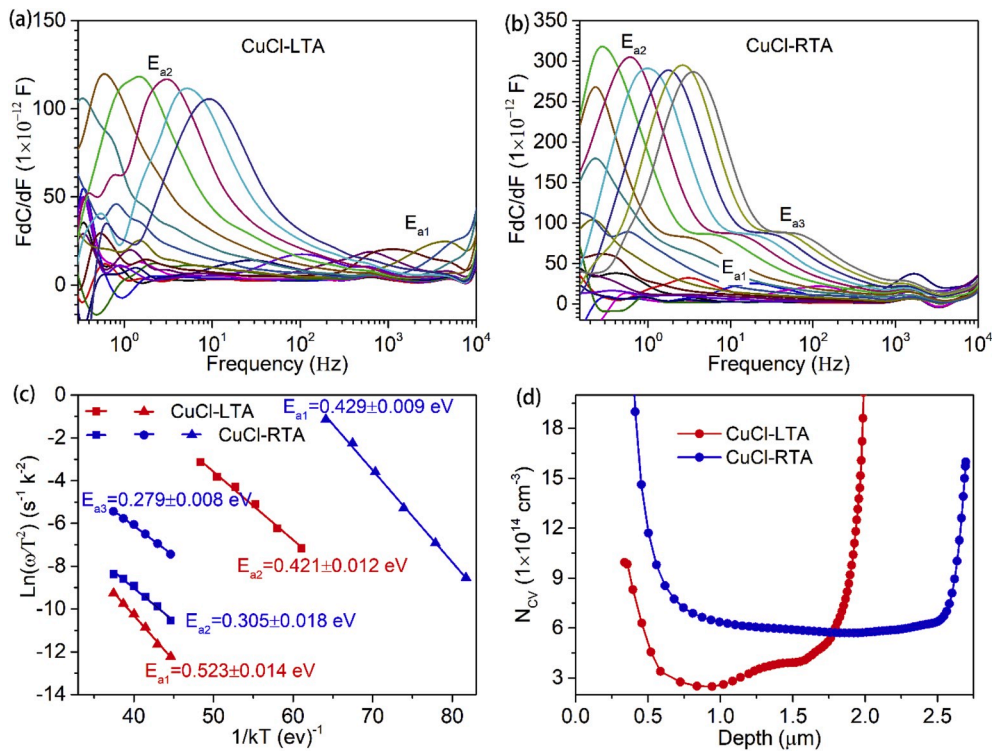


**Fig. 4.** Differential capacitance spectra ( $-FdC/dF$ ) at different temperatures in dark ( $V_{DC} = 0$  V), extracted from the capacitance spectra in Fig. S9, for (a) CuCl-LTA and (b) CuCl-RTA devices. (c) Arrhenius plots of admittance spectroscopy signature. (d) Carrier concentration as a function of the distance from the p-n junction calculated from the fitting curve of Mott-Schottky plot (Fig. S11) for devices with the LTA and RTA treatments.

by the ZMO layers. The CuCl-RTA device shows higher PL intensities than that for the CuCl-LTA device for excitations from both the glass and CdTe sides, indicating higher recombination rates in the CuCl-LTA device at both the ZMO/CdTe interface and the CdTe back surface [38]. The TRPL results in Fig. 3c further confirm this conclusion by showing a relatively longer carrier lifetime of 4.1 ns for CuCl-RTA than 2.2 ns for the CuCl-LTA device when excited from the glass side. This difference is attributed to the variation of Cu distribution at the ZMO/CdTe interface as well as in the ZMO layer, which mainly affects the generation of deep donor defect complexes in CdTe and the conductivity of ZMO film near the interface as discussed in the SIMS results. The device with a higher ZMO conductivity should introduce a stronger band bending in the CdTe, depleting holes at the ZMO/CdTe interface and effectively reducing the interface recombination. When the excitation is from the film side, the CuCl-RTA device also shows a higher lifetime than that for the CuCl-LTA device. This is mainly because the CuCl-RTA device has a higher Cu distribution at the back side as indicated by the SIMS results. A higher carrier concentration at the back side of CdTe leads to a lower back-barrier at the CdTe/Au interface, and thus a lower recombination rate. A steady-state PL measurement at 9 K is also performed by a 532 nm laser at  $25 \text{ mW cm}^{-2}$  to study the defect properties at the ZMO/CdTe interface, as shown in Fig. 3d. Similar features are observed in both CdTe films, including the donor-acceptor-pair transition (DAP) peaks at  $1.572 \pm 0.006$  eV (Cl donor to  $V_{Cd}$  acceptor) and  $1.468 \pm 0.004$  eV (Cl donor to  $Cu_{Cd}$  acceptor) [39]. A higher PL peak intensity at  $1.468 \pm 0.004$  eV indicates a higher number of  $Cu_{Cd}$  acceptors at the front interface in CdTe-RTA devices, although the CdTe-LTA devices reserve more Cu at the front interface. This is because excess Cu may introduce donor defects, i.e.,  $Cu_i$  rather than the more desired  $Cu_{Cd}$  acceptors in the CuCl-LTA device. This is confirmed by the higher PL intensity of the  $1.398 \pm 0.002$  eV defect peak for the CuCl-LTA device. The PL peak at  $1.398 \pm 0.002$  eV is observed by C. Corwine after Cu diffusion in single-crystal CdTe and assigned to the Cu related donor defects [40], possibly  $Cu_i$  related donor complex ( $O_{Te}-Cu_i$ ) [41]. This implies that

more hole trap states are formed at the front interface after the LTA treatment, lowering the minority carrier lifetime and PL intensity.

The defects states in CuCl-LTA and CuCl-RTA devices are further investigated through thermal admittance spectroscopy (TAS) measurements (Fig. 4). In the TAS curves (Fig. S9), the CuCl-RTA device shows a much higher capacitance at each temperature than the CuCl-LTA device, indicating more efficient carrier collection due to the lower recombination rate [42]. In the CuCl-LTA device, two transition frequencies are observed, and two activation energies ( $E_a$ ) are extracted (Fig. 4c) [43], including  $E_{a1} = 0.523 \pm 0.014$  eV and  $E_{a2} = 0.421 \pm 0.012$  eV. Whereas for the CuCl-RTA device, three transition frequencies can be clearly observed. The calculated activation energies are  $E_{a1} = 0.429 \pm 0.009$  eV,  $E_{a2} = 0.305 \pm 0.018$  eV, and  $E_{a3} = 0.279 \pm 0.008$  eV.  $E_{a1}$  for both devices are most likely due to the hole trap defects (H2-type) and can be assigned to the back-barrier height. The back-barrier heights are also calculated from the dark temperature-dependent J-V measurements (Fig. S10),  $0.644 \pm 0.012$  eV for CuCl-LTA and  $0.439 \pm 0.012$  eV for CuCl-RTA, respectively, consistent with  $E_{a1}$  measured from the TAS measurement. Both the capacitance and dark J-V measurements imply that the CuCl-RTA device shows a much smaller back-barrier height than the CuCl-LTA device, indicating a higher hole concentration at the back of CdTe film in the CuCl-RTA device. This is because the CuCl-RTA device reserves a higher Cu concentration at the back side than the CuCl-LTA device, as shown in the SIMS results. The reduction of the back-barrier height is beneficial to the improvements in  $V_{OC}$  and FF.  $E_{a2}$  and  $E_{a3}$  are possibly defects related to Cu [44]. This is because all the procedures for both devices are identical except the Cu treatment.  $E_{a2}$  ( $0.421 \pm 0.012$  eV) in CuCl-LTA is close to a deep acceptor-like defect ( $0.43$  eV), which has been assigned to an unknown Cu related defects [33].  $E_{a2}$  ( $0.305 \pm 0.018$  eV) and  $E_{a3}$  ( $0.279 \pm 0.008$  eV) in CdCl-RTA are close to acceptor  $Cu_{Cd}$  ( $\sim 0.3$  eV) [8,14]. In the device with the LTA treatment, the defect level of  $0.439 \pm 0.012$  eV is much deeper than either  $0.305 \pm 0.018$  eV or  $0.279 \pm 0.008$  eV in the CuCl-RTA device. The reduction in carrier trap state energy level can suppress the

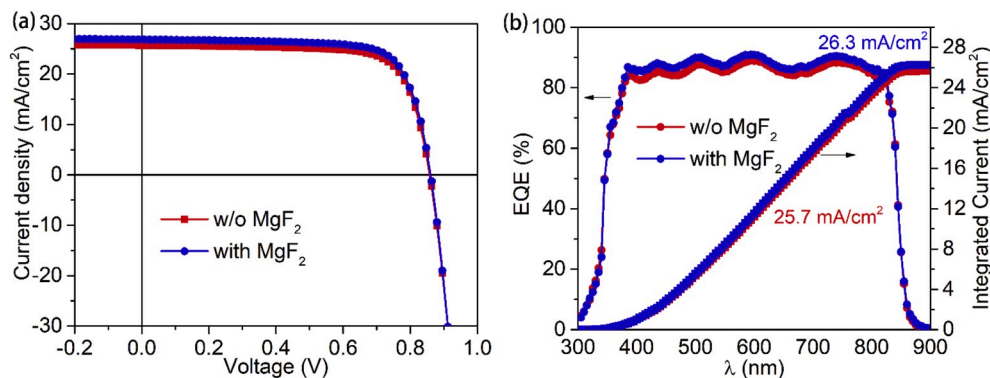


Fig. 5. (a) J-V and (b) EQE curves of the champion cell before and after the addition of a  $\text{MgF}_2$  anti-reflective layer.

nonradiative recombination in the device and help boost higher device performance. We further investigated the carrier concentration ( $N_A$ ) and the depletion width ( $W$ ) in the devices with the LTA and RTA treatments (Fig. 4d) based on the Mott Schottky plots of capacitance-bias ( $C-V$ ) measurements at room temperature (Fig. S11). The CuCl-RTA device shows a much higher carrier density ( $5.99 \times 10^{14} \text{ cm}^{-3}$ ) than the CuCl-LTA device ( $5.03 \times 10^{14} \text{ cm}^{-3}$ ) as well as a wider depletion width. This is beneficial for the higher built-in potential at the heterojunction, i. e., a higher  $V_{OC}$  and better device performance. To investigate the net Cu concentration in our devices, we performed an inductively coupled plasma mass spectrometry (ICP-MS) measurement on our saturated CuCl solution and obtained a Cu concentration of  $3.10 \mu\text{g ml}^{-1}$ . This value is much lower than the solubility of  $\text{CuCl}_2$  in ethanol ( $0.53 \text{ g ml}^{-1}$ ), indicating a facile way to control the Cu dosage using CuCl solutions. In our champion devices, an  $80 \mu\text{l}$  solution is used on  $1.5'' \times 1.5''$  CdTe films and the equivalent Cu atom concentration is about  $4.6 \times 10^{17} \text{ cm}^{-3}$  and the calculated equivalent metallic Cu thickness is estimated to be  $0.19 \text{ \AA}$ , which is about 157 times thinner than  $3 \text{ nm}$  Cu commonly applied through thermal evaporation. This is also the lowest Cu concentration doped in CdTe solar cells among previous reports. According to the carrier concentrations obtained from the  $C-V$  measurements, a Cu utility ratio of  $1/768$  is obtained in a CuCl-RTA device, which is higher than the value ( $1/915$ ) in a CuCl-LTA device and also much higher than the value ( $1/20,000$ ) in traditional devices with metallic Cu.

All the above results show that both Cu concentration and distribution can be engineered using the CuCl solution accompanied with the RTA treatment, which help to maximize the device performances with a minimal Cu concentration and an optimal Cu distribution. For our champion device, a  $120 \text{ nm}$  magnesium fluoride ( $\text{MgF}_2$ ) anti-reflective layer is deposited by e-beam evaporation. With  $\text{MgF}_2$ , the  $J_{SC}$  is improved by almost  $1 \text{ mA cm}^{-2}$  with the highest quantum efficiency of around 90%. This further enables the improvement of our champion device performance to a PCE of 17.5%, with a  $V_{OC}$  of  $0.861 \text{ V}$ , a  $J_{SC}$  of  $26.9 \text{ mA cm}^{-2}$  and a FF of 75.4%, as shown in Fig. 5, which is close to reported record CdTe devices without selenium incorporation [28].

#### 4. Conclusions

In this work, we report the use of a CuCl solution treatment for Cu activation for the first time and the lowest reported Cu concentration  $4.6 \times 10^{17} \text{ cm}^{-3}$  is achieved in our champion devices. Thus, the compensative donor-like defects ( $\text{Cu}_i$ ) at grain boundaries are suppressed. In addition, a rapid thermal annealing process is used to subtly confine most of the Cu atoms at the back side of CdTe film, thus, significantly reducing the recombination centers and shunt pathways at front interfaces. Combining the application of CuCl solution and RTA treatment, both the distribution and concentration of Cu in CdTe absorbers are well controlled, enabling the best-performing device with an efficiency of 17.5%, a  $V_{OC}$  of  $0.861 \text{ V}$ , a  $J_{SC}$  of  $26.9 \text{ mA cm}^{-2}$ , and a FF of

75.4%, which is among the highest CdTe device efficiencies without selenium incorporation.

#### Declaration of competing interest

The authors declare that they have no known competing financial interests or personal relationships that could have appeared to influence the work reported in this paper.

#### CRediT authorship contribution statement

**Deng-Bing Li:** Conceptualization, Data curation, Formal analysis, Investigation, Writing - original draft. **Sandip S. Bista:** Investigation. **Zhaoning Song:** Formal analysis, Writing - review & editing. **Rasha A. Awni:** Validation. **Kamala K. Subedi:** Validation. **Niraj Shrestha:** Validation. **Puja Pradhan:** Resources. **Lei Chen:** Investigation. **Ebin Bastola:** Validation. **Corey R. Grice:** Investigation. **Adam B. Phillips:** Resources. **Michael J. Heben:** Resources. **Randy J. Ellingson:** Resources. **Yanfa Yan:** Conceptualization, Data curation, Formal analysis, Funding acquisition, Project administration, Resources, Supervision, Writing - review & editing

#### Acknowledgments

This work is supported by Air Force Research Laboratory, Space Vehicles Directorate (contract # FA9453-18-2-0037) and National Science Foundation under contract no. 1665028 and 1711534. We thank Dr. David Strickler from Pilkington North America Inc. for supplying us FTO coated substrates.

#### Appendix A. Supplementary data

Supplementary data to this article can be found online at <https://doi.org/10.1016/j.nanoen.2020.104835>.

#### References

- [1] R.A. Awni, D.-B. Li, C.R. Grice, Z. Song, M.A. Razzoqi, A.B. Phillips, S.S. Bista, P. J. Roland, F.K. Alfadhili, R.J. Ellingson, M.J. Heben, J.V. Li, Y. Yan, *Solar RRL* 3 (2019) 1800304.
- [2] B.G. Mendis, Q.M. Ramasse, T.P. Shalvey, J.D. Major, K. Durose, *ACS Appl. Energy Mater.* 2 (2019) 1419–1427.
- [3] M.A. Green, Y. Hishikawa, E.D. Dunlop, D.H. Levi, J. Hohl-Ebinger, A.W.Y. Ho-Baillie, *Prog. Photovoltaics Res. Appl.* 26 (2018) 3–12.
- [4] T. Ablekim, C. Perkins, X. Zheng, C. Reich, D. Swanson, E. Colegrove, J.N. Duenow, D. Albin, S. Nanayakkara, M.O. Reese, T. Shimpi, W. Sampath, W.K. Metzger, *IEEE J. Photovolt.* 9 (2019) 888–892.
- [5] J. Huang, D. Yang, W. Li, J. Zhang, L. Wu, W. Wang, *Appl. Surf. Sci.* (2019) 253, <https://doi.org/10.1016/j.apsusc.2019.03>.
- [6] T.A.M. Fiducia, B.G. Mendis, K. Li, C.R.M. Grovenor, A.H. Munshi, K. Barth, W. S. Sampath, L.D. Wright, A. Abbas, J.W. Bowers, J.M. Walls, *Nat. Energy* (2019), <https://doi.org/10.1038/s41560-019-0389-z>.

- [7] E.I. Adirovich, Y.M. Yuabov, G.R. Yagudaev, *Sov. Phys. Semiconduct.* 3 (1969) 61–64.
- [8] S.-H. Wei, S.B. Zhang, *Phys. Rev. B* 66 (2002) 155211.
- [9] D. Krasikov, A. Knizhnik, B. Potapkin, S. Selezneva, T. Sommerer, *Thin Solid Films* 535 (2013) 322–325.
- [10] H.H. Woodbury, M. Aven, *J. Appl. Phys.* 39 (1968) 5485–5488.
- [11] E.D. Jones, N.M. Stewart, J.B. Mullin, *J. Cryst. Growth* 117 (1992) 244–248.
- [12] E. Bastola, A.V. Bordovalos, E. LeBlanc, N. Shrestha, M.O. Reese, R.J. Ellingson, *IEEE 46th Photovoltaic Specialists Conference, PVSC*, 2019, 2019 1846–1850.
- [13] Y. Yan, K. Jones, J. Zhou, X. Wu, M. Al-Jassim, *MRS Proc* 1012 (2011), 1012-Y1004-1009.
- [14] J. Perrenoud, L. Kranz, C. Gretener, F. Pianezzi, S. Nishiwaki, S. Buecheler, A. N. Tiwari, *J. Appl. Phys.* 114 (2013) 174505.
- [15] K.K. Chin, T.A. Gessert, S. Wei, *35th IEEE Photovoltaic Specialists Conference*, 2010, 2010 001915-001918.
- [16] N.R. Paudel, Y. Yan, *Thin Solid Films* 549 (2013) 30–35.
- [17] N.R. Paudel, C. Xiao, Y. Yan, *J. Mater. Sci-mater. El.* 25 (2014) 1991–1998.
- [18] D. Grecu, A.D. Compaan, *Appl. Phys. Lett.* 75 (1999) 361–363.
- [19] C.R. Corwine, A.O. Pudov, M. Gloeckler, S.H. Demtsu, J.R. Sites, *Sol. Energ. Mat. Sol. Cell* 82 (2004) 481–489.
- [20] K.D. Dobson, I. Visoly-Fisher, G. Hodes, D. Cahen, *Sol. Energ. Mat. Sol. Cell* 62 (2000) 295–325.
- [21] H. Song, X. Wu, J. Zheng, Q. Yan, *Asia-Pacific Power and Energy Engineering Conference*, 2010, 2010 1-4.
- [22] C. Li, H. Xu, K. Li, X. Ma, L. Wu, W. Wang, J. Zhang, W. Li, B. Li, L. Feng, *J. Electron. Mater.* 47 (2018) 1250–1258.
- [23] Y. Yang, T. Wang, C. Liu, W. Li, J. Zhang, L. Wu, G. Zeng, W. Wang, M. Yu, *Vacuum* 142 (2017) 181–185.
- [24] S. Uličná, P.J.M. Isherwood, P.M. Kaminski, J.M. Walls, J. Li, C.A. Wolden, *Vacuum* 139 (2017) 159–163.
- [25] J. Tang, D. Mao, T.R. Ohno, V. Kaydanov, J.U. Trefny, *Conference Record of the Twenty Sixth IEEE Photovoltaic Specialists Conference*, 1997, pp. 439–442.
- [26] E. Artegiani, D. Menossi, H. Shiel, V. Dhanak, J.D. Major, A. Gasparotto, K. Sun, A. Romeo, *Prog. Photovoltaics Res. Appl.* 27 (8) (2019) 706–715.
- [27] J. Sites, A. Munshi, J. Kephart, D. Swanson, W.S. Sampath, *IEEE 43th Photovolt Spec Conf* (2016) 3632–3635.
- [28] A.H. Munshi, J. Kephart, A. Abbas, J. Raguse, J. Beaudry, K. Barth, J. Sites, J. Walls, W. Sampath, *IEEE J. Photovolt.* 8 (2018) 310–314.
- [29] N.R. Paudel, C. Xiao, Y. Yan, *Prog. Photovoltaics Res. Appl.* 23 (2015) 437–442.
- [30] D.-B. Li, X. Yin, C.R. Grice, L. Guan, Z. Song, C. Wang, C. Chen, K. Li, A.J. Cimaroli, R.A. Awni, D. Zhao, H. Song, W. Tang, Y. Yan, J. Tang, *Nano Energy* 49 (2018) 346–353.
- [31] N.R. Paudel, J.D. Poplawsky, K.L. Moore, Y. Yan, *IEEE J. Photovolt.* 5 (2015) 1492–1496.
- [32] J.R. Sites, P.H. Mauk, *Sol. Cell.* 27 (1989) 411–417.
- [33] A. Balcioglu, R.K. Ahrenkiel, F. Hasoon, *J. Appl. Phys.* 88 (2000) 7175–7178.
- [34] Y. Deng, J. Yang, R. Yang, K. Shen, D. Wang, D. Wang, *AIP Adv.* 6 (2016), 015203.
- [35] T.R.N. Kutty, N. Raghu, *Appl. Phys. Lett.* 54 (1989) 1796–1798.
- [36] C.X. Xu, X.W. Sun, X.H. Zhang, L. Ke, S.J. Chua, *Nanotechnology* 15 (2004) 856–861.
- [37] A. Hausmann, B. Schallenger, R. Roll, *Z. Phys. B* 40 (1980) 1–7.
- [38] D.-B. Li, Z. Song, R.A. Awni, S.S. Bista, N. Shrestha, C.R. Grice, L. Chen, G. K. Liyanage, M.A. Razooqi, A.B. Phillips, M.J. Heben, R.J. Ellingson, Y. Yan, *ACS Appl. Energ. Mater.* 2 (2019) 2896–2903.
- [39] H. Opyrchal, D. Chen, Z. Cheng, K. Chin, *Coatings* 9 (2019) 435.
- [40] C. Corwine, J. Sites, T. Gessert, W. Metzger, P. Dippo, A. Duda, *APS Four Corners Section Meeting Abstracts*, Tempe (2003).
- [41] C.R. Corwine, J.R. Sites, T.A. Gessert, W.K. Metzger, P. Dippo, J. Li, A. Duda, G. Teeter, *Appl. Phys. Lett.* 86 (2005) 221909.
- [42] H.-S. Kim, D.B. Patel, H. Kim, M. Patel, K.R. Chauhan, W. Park, J. Kim, *Sol. Energ. Mat. Sol. Cell* 164 (2017) 7–12.
- [43] M.J. Koeper, C.J. Hages, J.V. Li, D. Levi, R. Agrawal, *Appl. Phys. Lett.* 111 (2017) 142105.
- [44] R.A. Awni, D.-B. Li, Z. Song, S.S. Bista, M.A. Razooqi, C.R. Grice, L. Chen, G. K. Liyanage, C. Li, A.B. Phillips, M.J. Heben, R.J. Ellingson, J.V. Li, Y. Yan, *Prog. Photovoltaics Res. Appl.* 27 (2019) 1115–1123.